PCCP

ROYAL SOCIETY OF CHEMISTRY

PAPER

View Article Online
View Journal | View Issue

Cite this: *Phys. Chem. Chem. Phys.*, 2024, **26**, 13383

New insights into the photocyclization reaction of a popular diarylethene switch: a nonadiabatic molecular dynamics study†

Mikołaj Martyka [ab] and Joanna Jankowska *[a]

Received 22nd December 2023,
Accepted 4th April 2024

DOI: 10.1039/d3cp06256b

rsc.li/pccp

Diarylethene (DAE) molecular switches have continued to attract the attention of researchers for over 20 years. Their remarkable photophysical properties endow them with countless applications in photonics and molecular technologies. However, despite extensive experimental and theoretical research, the mechanism of DAE photoswitching is not yet fully rationalized. In this work, we investigate the ring closure dynamics of a popular DAE switch, 1,2-bis(3-methyl-5-phenyl-2 thienyl)perfluorocyclopentene (PT), using nonadiabatic molecular dynamics (NAMD) simulations. Employing the fewest switches surface hopping protocol, along with the semi-empirical multireference ODM2/MRCI-SD method, we investigate possible reaction pathways for this photoprocess, as well as their timescales and resulting photoproducts. Furthermore, using a dynamic configuration-space sampling procedure, we elucidate the role of triplet states in the photocyclization of PT, supporting available experimental data for the closely related DMPT molecule, which indicate an ultrafast intersystem crossing (ISC) transition competing with the singlet-driven photoswitching reaction. Our findings not only corroborate experimental studies on DAE switches, but also provide new mechanistic insights into the potential use in the rational design of DAE switches tailored for specific technological applications.

1 Introduction

Diarylethenes (DAEs) are an outstanding family of molecular switches, with numerous applications in fundamental science and new technologies.[1–5] They are known for their high thermal stability,[6] fatigue resistance[7–9] and ultra-fast response time.[10–12] Furthermore, they can be synthesised with relative ease,[13] and are reactive in a variety of environments, including a wide range of solvents, gels, crystals, and nanoparticles.[14–16]

Upon exposure to light, DAE compounds undergo a 6π, thermally irreversible[16,17] photocyclization/cycloreversion reaction, switching between an open-ring, hexatriene-based isomer (OF), and a closed-ring, cyclohexadiene-like form (CF). The UV-induced cyclization reaction can be reversed under excitation of the closed form in the visible range. The photoswitching cycle of DAEs is schematically shown in Fig. 1. For most DAE molecules, two ground-state conformers of the OF exist in equilibrium: a parallel (P) rotamer, with the two side-rings being mirror reflections of each other (C_s symmetry), and an anti-parallel (AP) rotamer, exhibiting C_2 symmetry.[18–20] Because of the Woodward–Hoffman rules,[21,22] only the AP rotamer is

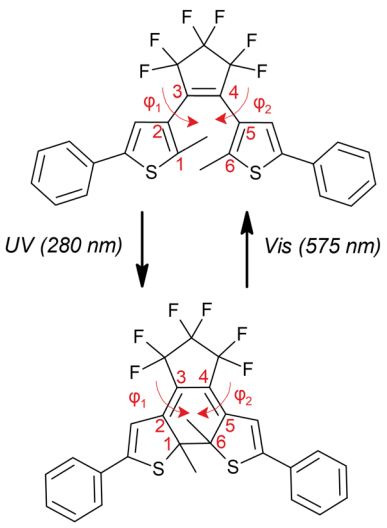

Fig. 1 Photoswitching forms of PT, along with typical excitation wavelengths used in the experiment, and with a definition of dihedral angles relevant in the photorelaxation process: φ_1 (C_1C_2–C_3C_4) and φ_2 (C_6C_5–C_3C_4).

[a] *Faculty of Chemistry, University of Warsaw, Pasteura 1, Warsaw, 02-093, Poland. E-mail: jjankowska@chem.uw.edu.pl*
[b] *Interdisciplinary Doctoral School, University of Warsaw, Dobra 56/66, Warsaw, 00-312, Poland*

† Electronic supplementary information (ESI) available. See DOI: https://doi.org/10.1039/d3cp06256b

reactive in the photoswitching process. Both the cyclization and cycloreversion processes are assumed to proceed through a common conical intersection, involving breaking/formation of the central C_1–C_6 bond between the reactive carbon atoms.[11,23,24]

Among numerous photoswitches belonging to the DAE family, 1,2-bis(3-methyl-5-phenyl-2 thienyl)perfluorocyclopentene, commonly referred to as PT, and closely related DMPT (1,2-bis(2,4dimethyl-5-phenyl-3-thienyl)perfluorocyclopentene) stand out as particularly interesting photoswitches from both, pure and applied science, points of view. The photoswitching cycle of these systems is particularly highly biased: a trait exhibited to a certain extent by all DAE systems, meaning that the quantum yield of the photocyclization process is much higher than that of photocycloreversion. This property, along with outstanding fatigue resistance,[25] and a two-photon amplification of the cycloreversion quantum yield[23,24] allowed PT and DMPT to make their way into many technological applications,[26–28] as well as made them the object of numerous fundamental studies.[14,23,29]

Owing to its popularity, a rich set of dedicated experimental studies deliver high-quality data describing PT photochemistry and photophysics. The first absorption maximum of PT-OF is reported at 280 nm (4.42 eV) in *n*-hexane,[30] while PT-CF typically absorbs at 575 nm (2.16 eV).[14,23,31] The closed-form isomer of PT exhibits weak fluorescence, emitting at 780–800 nm, when irradiated with 580 nm light.[23] Fluorescence of the OF is much stronger, with a maximum at around 425 nm, upon 300 nm excitation. However, this open-isomer emission is attributed solely to the unreactive P conformer.[32] The total photocyclization quantum yield of PT, $\Phi_{OF\rightarrow CF}$, is reported to be 59%,[14] which, after taking into account the actual fraction of the AP conformer, assumed to be *ca.* 0.6–0.7,[23] translates to a quantum yield of around 90% per reactive AP molecule. On the other hand, the photocycloreversion yield of PT is exceptionally low, given at 1.3%.[14,23,33] The cycloreversion process occurs on a timescale of *ca.* 12 ps,[23] while the cyclization reaction is known to be ultra-fast, with sub-picosecond timescales reported for numerous DAE compounds,[34] including 300 fs for DMPT.[35] Until recently, both, the cyclization and the cycloreversion processes, were assumed to take place only within the singlet manifold of states. However, Hamdi *et al.* in their 2016 paper raised questions about this, discovering an unexpected and fast intersystem crossing process during the cyclization dynamics of the AP conformer of DMPT-OF.[36] Conversely, the unreactive P isomer is reported as phosphorescent, decaying at a microsecond timescale, after a fast (22 ps in DMPT) intersystem crossing from the S_1 state.[35,36]

Despite numerous difficulties arising from the complexity of the discussed photoprocess, several theoretical investigations have provided high-level insights into DAE photoswitching. The pioneers in this field were Nakamura and Irie in 1988, discovering a connection between the energy difference of the OF and CF isomers and the thermal stability of the system, using the semi-empirical MNDO method.[37] A couple of years later, Majumundar *et al.*[38] used the TD-DFT methodology with the B3LYP functional to study the impact of the Franck–Condon (FC) vertical excitation energy difference between the two switching forms on the performance of DAE switches. Several later works, by Uchida *et al.*[39] and Asano *et al.*,[40] started utilizing the multireference methodology for the study of DAE systems. Relaxed complete active space self-consistent field (CASSCF) calculations, supplemented with single point complete active space perturbation theory of the second order (CASPT2) results, yielded an accurate description of the excited states participating in the cycloreversion reaction, at least in the vicinity of the closed-form Franck–Condon region. In 2013, a work by Perrier *et al.*[41] highlighted the necessity of including both static and dynamic electronic correlations for a proper description of the S_1 and S_2 states. Recently, the photoswitching of DAE systems was studied at the TD-DFT,[42] spin–flip TD-DFT,[43] and semi-empirical[44] levels of theory, with reported relaxed potential energy profile scans along the reaction coordinate. Several studies investigated this photo-reaction by means of molecular dynamics;[45–47] however, due to the size and demanding nature of the system, they were only limited to model, truncated molecules. Recently, our group conducted the first study of a full-size DAE system using on-the-fly nonadiabatic molecular dynamics, which stood in good agreement with available experimental data.[48]

The aim of this investigation is to provide theoretical insights into the photocyclization reaction of PT at a previously unavailable dynamic level. To achieve this, we employ the cutting-edge ODM2/MRCI-SD semi-empirical methodology, coupled with the tried-and-true fewest switches surface hopping algorithm, to investigate the possible reaction pathways, and conical intersections through which they proceed, the timescales, as well as the formed photoproducts. Furthermore, an analysis of intersystem crossing effects is performed, using a dynamic configuration-space sampling procedure, allowing for the inclusion of vibronic effects, in order to provide comprehensive insights into the role of triplet states in the PT photocyclization process.

This manuscript is organised in the following order: the Computational details section outlines the employed computational methods and protocols, as well as their settings. Next, in the Results and discussion section, the results of the investigation are presented, including: (1) characterization of the ground-state minima, relevant in the photoswitching process; (2) NAMD simulations of the PT cyclization process; (3) photophysics of the unreactive PT-twist form, and its potential ISC mechanism to the triplet manifold of states. The findings are summarised in the Conclusions section.

2 Computational details

2.1 Electronic structure methods

2.1.1 Semi-empirical methods. In this contribution, the method of choice for computing the electronic structure of PT is the semi-empirical ODM2/MRCI-SD approach:[49–52] the orthogonalization and dispersion corrected multireference configuration interaction method, including single and double

excitations within the active space. Calculations were performed using the MNDO99 program (v7 with upgrades).[53] This method, along with the similar OM2 and OM3 models, has been successfully employed in the description of many photoactive systems,[54–57] including DAE[44,48] and closely related fulgides.[58,59]

In all ODM2/MRCI-SD calculations, the half-electron restricted open-shell Hartree–Fock formalism[60] was applied for the initial SCF step, with two singly occupied orbitals: the HOMO and the LUMO. During the MRCI calculations, the SCF configuration (of singlet multiplicity for calculations within the singlet manifold of states, and triplet when the system is within the triplet manifold of states) was supplemented with two additional reference state functions: the closed shell HOMO–HOMO and doubly excited LUMO–LUMO configurations. The MRCI-SD procedure included all single and double electronic excitations from these references, restricted to electron transfers from and to orbitals included in the active space (AS). The AS consisted of 6 electrons in 8 orbitals in all semi-empirical calculations, and was previously tested by our group for closely related DAE systems.[44] Contour plots of the AS orbitals can be found in Section S1 of the ESI,† while the Cartesian coordinates of all optimized minima, as well as minimum-energy conical intersection points, can be found in Section S7 of the ESI.† Through this study, we have chosen to keep the ODM2/MRCI-SD orbital active space equal in size between different forms of PT. Due to this fact, the chosen active space may not always conform to the approximate symmetry of the given PT isomer. However, this factor does not impact the geometrical conformation of PT in a substantial manner, as supporting DFT optimizations (discussed in Section 2.1.2) remain in very good agreement with the ODM2/MRCI-SD results.

2.1.2 *Ab initio* calculations. To provide accurate means of evaluating the electronic structure and spin–orbit coupling matrix elements in the dynamic sampling procedure, the quasi-degenerate second order n-electron valence state perturbation theory (QD-NEVPT2) was used,[61,62] as implemented in the ORCA 5.0.3 quantum chemistry package.[63,64] The initial CASSCF step was performed with an AS of 8 electrons in 8 orbitals, to enhance numerical stability in the CASSCF calculation, with equal-weight state averaging over T_1, S_0, S_1, and S_2. In these calculations, the Dunning correlation-consistent double-ζ basis set[65] was utilised, with the auxiliary basis set generated automatically.[66] Contour plots of the final, optimized orbitals can be found in the ESI,† in Section S2.

The spin–orbit coupling matrix elements (SOC-MEs) were computed using the spin–orbit mean-field (SOMF) approximation,[67–69] using ORCA, with the inclusion of one-electron terms, exact Coulomb terms, and exchange terms modelled by exact one-centre integrals including the spin–other orbit interaction (corresponding to the SOCFlags option set to 1,4,3,0). The magnitude of the SOC-ME reported throughout this manuscript is obtained by taking the module square of the coupling vector.

The structures of the studied S_0 and S_1 minima were benchmarked at the density functional theory level. For the ground-state minima, as well as in the excited-state TD-DFT calculations, structural reoptimizations were performed using the range-separated hybrid ωB97X-D functional,[70] again combined with the cc-pVDZ basis set. The Tamm–Dancoff approximation (TDA)[71] was used in all TD-DFT calculations. A detailed analysis of the DFT benchmark data can be found in Section S3 in the ESI,† along with the Cartesian coordinates of all the reoptimized molecular structures. Furthermore, the obtained agreement between DFT and semi-empirical optimizations in the geometrical parameters of PT may be used as a validation of the chosen AS in ODM2/MRCI-SD calculations.

2.2 Nonadiabatic molecular dynamics

For the propagation of the nonadiabatic molecular dynamics, Tully's fewest switches surface hopping (FSSH)[72,73] algorithm was used, as implemented in the MNDO99 package, with orbital phase tracking between the consecutive dynamics steps. Initial conditions were sampled from a 4 ps microcanonical-ensemble molecular dynamics (MD), which was preceded by a 4 ps thermalization run within the canonical ensemble. Sampling initial conditions from the ground-state Born–Oppenheimer molecular dynamics (BOMD) allow for a straightforward inclusion of finite-temperature effects and anharmonic vibrational contributions into the initial conditions, making the BOMD the method of choice for a system like PT, expected to be heavily influenced by large-amplitude side-ring vibrations and rotations.

A 298 K Nose–Hoover thermostat[74] with a chain length of 10 and a characteristic time of 0.05 ps was used in the thermalization step. The time step for the nuclear motion was set to 0.5 fs in all dynamic simulations. In the initial conditions generation procedure, the starting points (molecular structures and atomic velocities) were filtered according to the optical transition probability, with an excitation energy window of 4.10 ± 0.15 eV, using the following equation:[75]

$$P = \frac{f/\Delta E^2}{\max(f/\Delta E^2)} \quad (1)$$

where f is the oscillator strength for the transition, ΔE is the energy gap between the states, and the value in the denominator is the maximum ratio of f to ΔE^2 in all the sampled geometries. Then, a random number $0 < p < 1$ was generated. If $p \leq P$, the geometry is included in the initial condition set; otherwise, it is rejected. Trajectories used for the investigation of the photophysical properties of the PT-twist were randomly sampled from a 4 ps microcanonical MD run in the S_1 state and started without further filtering.

Eventually, a set of 168 (125) NAMD trajectories were run in the PT-OF (PT-twist) dynamics. The maximum propagation times were set to 1800 fs and 2000 fs, respectively. All relevant properties, such as gradients and nonadiabatic coupling (NAC), were obtained analytically on-the-fly at the ODM2/MRCI-SD level. Electronic motion was propagated using the unitary propagator evaluated at the middle point,[76] with electronic structure integration performed every 0.0025 fs. The adaptive time step algorithm[77] was also employed, with an energy change threshold set to 0.01%, and a maximum number of

step reductions of 10. Decoherence was accounted for using Shenvi–Subotnik's parameterless correction and the phase of the AS orbitals was tracked between subsequent NAMD steps.[78] To ensure energy conservation, nuclear velocities were rescaled after hopping, along the direction of the NAC vector. Frustrated hops (with the nuclear velocity component along the NAC vector too small to compensate for the energy change due to surface switching) were rejected, and the velocity along the NAC vector was reversed.

To explicitly account for vibronic effects impact on the intersystem crossing during the PT photorelaxation, a procedure of dynamic configuration-space sampling was applied. From each of the 125 PT-twist NAMD trajectories, 30 snapshots were randomly selected and used for the evaluation of molecular properties. In this protocol, spin–orbit coupling matrix elements, as well as energies of the T_1, S_0, S_1, and S_2 states were determined at the QD-NEVPT2 level of theory in a single-point manner. From the total of 3750 sampled geometries, 1624 were discarded due to numerical errors, leaving 2126 samples available for analysis.

2.3 Data analysis

This work follows a two-letter convention for naming electron configurations appearing in the configuration interaction expansion: A–B denotes a configuration in which an electron was removed from orbital(s) A and placed on orbital B, with respect to the closed-shell HOMO–HOMO configuration. For example, H1–L1 is a configuration constructed by moving a single electron from the HOMO-1 orbital to the LUMO+1 orbital, and HH–LL is a doubly excited configuration, in which two electrons were moved from the HOMO to the LUMO.

Molecular dynamics-averaged electronic absorption spectra were obtained using a Lorentzian broadening:

$$L(x, x_0) = \frac{1}{2\pi}\frac{\Gamma}{(x - x_0)^2 + \frac{1}{4}\Gamma^2}, \tag{2}$$

where Γ is a predefined full-width at half-maximum parameter, set to 0.05 eV, and x_0 is the centre of the peak taken as the vertical excitation energy calculated at a given structure sampled from the initial microcanonical MD run. The spectra were prepared using all geometries generated in the 4 ps production MD run of PT-OF, and excitations to the first three singlet excited states were taken into account.

The reaction quantum yields, $\Phi_{A\rightarrow B}$, have been calculated as a fraction of trajectories relaxing to a given photoproduct (N_B), to the total number of trajectories starting from A and relaxing to S_0 (N_{traj}):

$$\Phi_{A\rightarrow B} = \frac{N_B}{N_{traj}}. \tag{3}$$

The statistical uncertainties of these yields, $\Delta\Phi$, were estimated using the normal approximation interval for a binomial process[79] which, for a confidence interval of 95%, takes the form:

$$\Delta\Phi = 1.96 \cdot \sqrt{\frac{\Phi(1-\Phi)}{N_{traj}}}. \tag{4}$$

The photo-deactivation timescales of PT-OF were extracted from the simulation data by fitting a double sigmoidal function, $P(t)$, to the rise of the electronic ground state population in time:

$$P(t) = \frac{A}{1 + e^{-B(t-\tau_1)}} + \frac{C}{1 + e^{-D(t-\tau_2)}}. \tag{5}$$

Here, τ_1 and τ_2 are the fitted relaxation timescales, A and C represent the fraction of the population relaxing on a given timescale, and B and D can be associated with the steepness of the growth curve for each timescale. The proposed $P(t)$ function has been chosen for its universality and has previously shown to provide parameters well-comparable with experimental data.[48,80]

3 Results and discussion

3.1 Ground-state properties of PT

In the first step of the investigation, ground-state minima of PT, corresponding to the open- and closed-ring isomers, were optimized at the ODM2/MRCI-SD level. In line with previous findings regarding DAE systems,[44] PT-OF proved to be the global minimum in S_0, with the PT-CF form less stable by 0.28 eV. The C_1–C_6 distance, which can be interpreted as a leading reaction coordinate in the photocyclization/cycloreversion process, takes values of 1.54 Å in PT-CF and 3.50 Å in PT-OF. In the CF minimum, the DAE core of the molecule remains relatively flat, with the φ_1 and φ_2 angles of 5 and 8 degrees. Conversely, in the OF form, the thiophene moieties lay at an angle with respect to the perfluoro-pentane ring, with φ_1 and φ_2 angles equal to 50 and 53 degrees. The discussed structures were reoptimized using DFT, as described in Section 2.1.2. The global-minimum character of the OF is maintained in the DFT calculations, with PT-OF being stabilized by 0.49 eV with respect to PT-CF. The obtained geometric structures match the ODM2/MRCI-SD minima very well, with the same predicted C_1–C_6 distance, and very similar values of the φ_1 and φ_2 dihedral angles, differing by no more than 5 degrees from the ODM2/MRCI-SD results.

The PT vertical absorption properties, computed at the semiempirical and *ab initio* levels of theory, are summarised in Table 1. For most diarylethene photoswitches, the first excited state is found bright, dominated by a H–L contribution. The second excited state is predicted to be dark, with contributions mainly from an H1–L configuration for PT-OF. For the closed-form, however, the S_2 wavefunction is predicted to be distinctly multiconfigurational, dominated by a doubly-excited HH–LL determinant. Compared to experiment,[30] for the OF isomer, both applied methods underestimate the absorption energy by *ca.* 0.3 eV (experimental value: 4.42 eV/280 nm), while a blue-shift of about 0.6 eV is observed for PT-CF at the semiempirical

Table 1 Vertical excitation energies (ΔE), oscillator strengths (f), and leading configuration contributions in the CI expansion (Orbs) for both photoswitching forms of PT, computed for geometries optimized at the ODM2/MRCI-SD level of theory. Approximate C_s-group state symmetries indicated in brackets.

	PT-OF			PT-CF		
	ΔE	f	Orbs	ΔE	f	Orbs
ODM2/MRCI-SD						
S_1	4.11 (B)	0.1462	H–L (92%)	2.77 (B)	0.2230	H–L (92%)
S_2	4.60 (A)	0.0640	H1–L (88%)	3.68 (A)	0.0033	HH–LL (50%) H1–L (22%), H–L1 (21%)
QD-NEVPT2						
S_1	4.07 (B)	0.2152	H–L (75%), H1–L (15%)	2.16 (B)	0.3871	H–L (88%)
S_2	4.57 (A)	0.0857	H1–L (72%), H–L (15%)	3.50 (A)	0.0010	HH–LL (48%) H–L1 (18%) H1–L (15%)

level, with *ab initio* yielding a fairly accurate value (2.16 eV/575 nm measured experimentally in *n*-hexane[14,23,31]). TD-DFT vertical excitation energies computed using DFT-optimized minima of PT predict PT-OF to absorb at ΔE = 4.37 eV (283 nm), which improves upon the ODM2/MRCI-SD and QD-NEVPT2 predictions; however, ΔE = 2.72 (456 nm) for PT-CF replicates the blue-shift obtained at the semi-empirical level.

3.2 NAMD simulation of the PT photocyclization process

In the next step, nonadiabatic dynamics runs, simulating the relaxation of PT-OF after the optical excitation, were performed. First, the dynamic, MD-averaged electronic spectra were prepared, as plotted in Fig. 2, along with marked individual contributions from the $S_0 \rightarrow S_x$ transitions. The overall shape of the absorption spectrum, as well as its secondary features, match the experimental data reasonably well with the previously indicated systematic energy shifts.

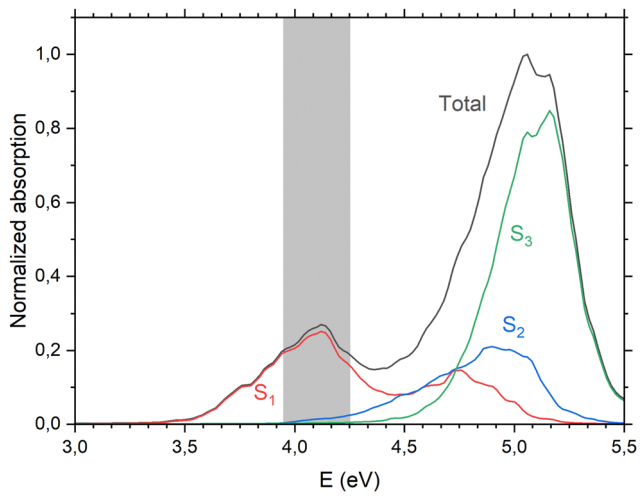

Fig. 2 Dynamic absorption spectrum of PT-OF, obtained from ground-state MD calculations. The contributions from the $S_0 \rightarrow S_1$, $S_0 \rightarrow S_2$, and $S_0 \rightarrow S_3$ transitions to the total spectral profile are marked in red, blue, and green, respectively. The excitation window used in the initial-condition filtering for PT-OF NAMD simulations has been shaded in grey.

3.2.1 Electronic-state population evolution. The evolution of the electronic state populations in the PT-OF dynamics is plotted in Fig. 3. Due to a certain degree of spectral overlap, a small portion of trajectories is initially excited to S_2 which, however, relaxes on an ultrashort timescale (*ca.* 40 fs) to the first excited state. In the course of the dynamics, several trajectories populate the second excited state through up-in-energy hops; yet their lifetime in S_2 is very short, usually below 20 fs. In the limit of large t (after around 1.3 ps), the S_0 population curve saturates, with almost no further relaxation events taking place. At the same time, a sizeable (6%) portion of trajectories remains in the electronic excited state. This behaviour hints at a possibility of competition between the internal conversion and other relaxation mechanisms, such as fluorescence and phosphorescence. This possibility will be explored in more detail later in the manuscript.

Characteristic timescales of the nonradiative relaxation were extracted from the simulation data by fitting a double-sigmoid decay curve, given by eqn (5). The parameters A and C can be interpreted as the fraction of the excited state population relaxing with timescales of τ_1 and τ_2, respectively. From the fitted parameters' values, given in Section S4 of the ESI,† along with their uncertainties, we can conclude that about 53% of the trajectories relax at a timescale of τ_1 = 342 fs, and 41% with τ_2 = 766 fs, while the remaining 6% remains primarily in the S_1 state. The fitted timescales stand in good agreement with the experimental data, which report the cyclization process occurring on a sub-picosecond timescale in most diarylethene derivatives.[12,34,35] Interestingly, the observed time interval between the two obtained timescales lies close to a characteristic excited-state DAE vibration (ν = 67 cm^{-1}; τ = 498 fs) involving anti-symmetric out-of-plane rocking of the thiophene rings about φ_1 and φ_2 which, in the vicinity of the S_1/S_0 conical intersection, has a strong impact on the S_1/S_0 energy gap.[40,45]

3.2.2 Photoproduct formation and quantum yields. The relaxation processes in the PT-OF dynamics can be associated with the presence of minimum-energy conical intersection (MECI) points, providing efficient gateways for the $S_1 \rightarrow S_0$ deactivation (panel (a) of Fig. 4). The majority of

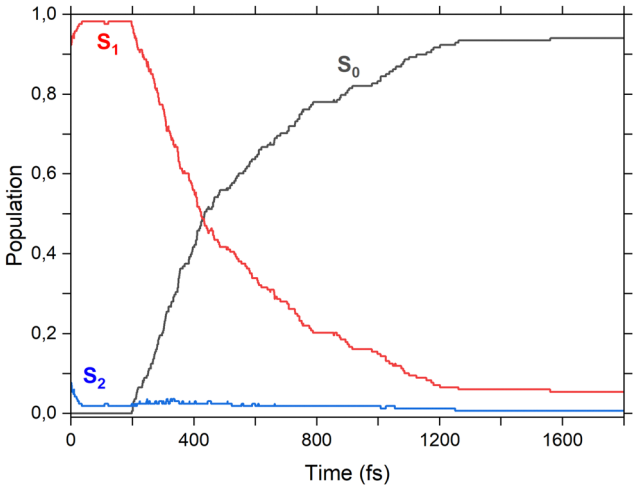

Fig. 3 Electronic state population evolution in the photo-cyclization dynamics of PT. The states S_0, S_1, and S_2 have been marked respectively in black, red, and blue.

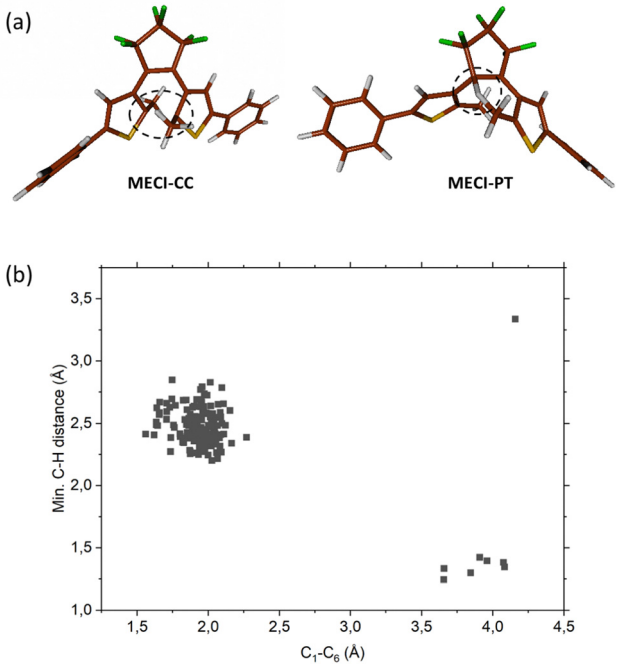

Fig. 4 Optimized MECI structures of the two conical intersections through which the PT-OF relaxation proceeds in the NAMD simulations. The characteristically distorted sites of the system have been marked with a dashed circle in both cases (a). Correlation plot for the C_1–C_6 length and the minimal distance between a hydrogen atom of the methyl group and the C_3/C_4 carbon atom to which the proton/hydrogen atom transfer takes place, at the $S_x \rightarrow S_0$ hopping point (b).

trajectories (89%) relax in the vicinity of a typical DAE MECI (**MECI-CC**), involving the formation/breaking of the C_1–C_6 bond and characterised by C_1–C_6 = 1.87 Å. A minor, yet noticeable part of NAMD trajectories (5%) relaxes through a previously unreported conical intersection involving a proton (or a hydrogen atom) transfer between the methyl group attached to one of the reactive carbon atoms and C_1/C_4 (**MECI-PT**). The relative contribution of both relaxation pathways correlates well with the MECI point adiabatic energies of 2.53 eV (**MECI-CC**) and 3.16 eV (**MECI-PT**). Upon inspection of the correlation plot showing the C_1–C_6 distance and the minimum distance between C_3/C_4 and a hydrogen atom attached to the methyl group (panel (b) of Fig. 4) at the moment of hopping to the S_0 state, one can notice that the system relaxation points indeed form two distinct clusters: (i) the first, characterised with small C_1–C_6 and large C–H, indicating deactivation proceeding through **MECI-CC** and (ii) the second, showing large C_1–C_6 and small C–H, corresponding to **MECI-PT**. The one outlier point showing high values of both parameters stems from a relaxation event through a high energy gap, which should be probably assumed an artefact of the employed FSSH methodology.

Of the 150 trajectories relaxing in the vicinity of **MECI-CC**, PT-OF and PT-CF are the only photoswitching products observed in the simulations. The closer inspection of trajectories relaxing *via* **MECI-PT** reveals that 3 of 7 such trajectories form an alternative photoproduct in which the hydrogen atom is permanently bonded to the C_5H_6 ring, whilst the remainder recreates PT-OF. This alternative deactivation channel can be thought of as a side process, lowering the cyclization quantum yield of the studied DAE system. It should be noted that an unequivocal distinction between a proton-transfer or a hydrogen atom-transfer nature of the observed process is hard to make in the studied case, since the proton-donating and proton-accepting moieties are directly conjugated electronically. Moreover, the existence and role of this deactivation channel may be dependent on the solvent used; this effect, however, was not investigated in the present study. The Cartesian coordinates of the optimized S_0 structure of this alternative photoproduct can be found in the ESI,† in Table S14. The $S_0 \rightarrow S_1$ transition energy of this new form is found to be 4.08 eV, making it practically indistinguishable from PT-OF in a simple UV-Vis absorption experiment, while the adiabatic energy of its optimized structure is found to be 0.62 eV relative to PT-OF.

In Fig. 5, one can find the distribution of the final C_1–C_6 distances, *i.e.*, distances measured in the last geometrical structure of every trajectory in the cyclization dynamics simulations. Taking C_1–$C_6 < 2.00$ Å as a fingerprint of the successful CF product formation and applying eqn (3), one can determine the total photocyclization quantum yield of $\Phi = 78 \pm 6\%$. This value corresponds reasonably with available experimental data, typically reporting a quantum yield of 96% per reactive PT-OF (AP) molecule (46% overall).[14,23] Moreover, if one excludes trajectories that relaxed to S_0 *via* **MECI-PT**, the theoretically estimated Φ value increases to $83 \pm 6\%$.

We now turn to the unrelaxed portion of trajectories, which remained in the excited state in the PT-OF dynamics. Structural analysis reveals that most of them (8 out of 10 trajectories) adopt a twisted geometry, PT-twist, with the thiophene-phenyl moieties being oriented perpendicularly with respect to the central ring, as shown in Fig. 6, resulting in the new, potentially unreactive OF conformation. This seems to remain in line

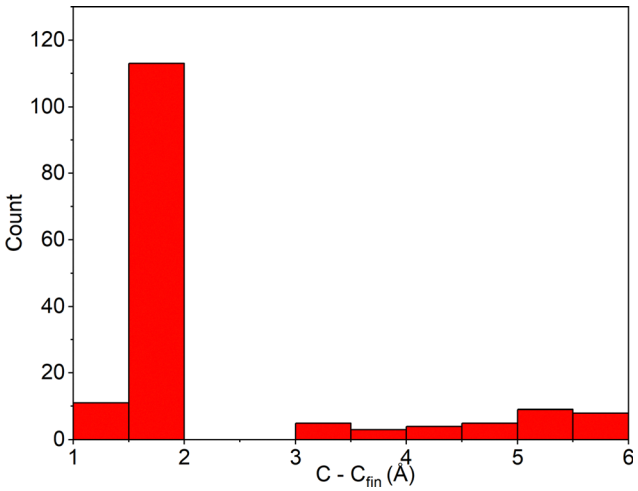

Fig. 5 C_1–C_6 distance distribution of trajectories that underwent deactivation to S_0, at the end of the photocyclization process of PT.

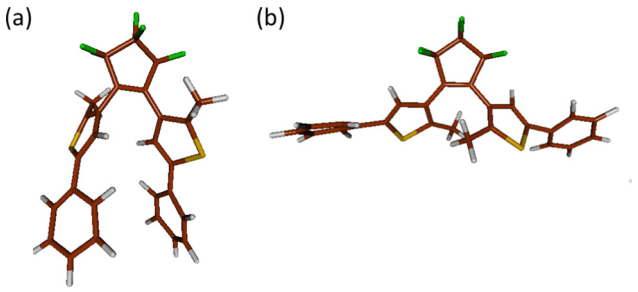

Fig. 6 A comparison of molecular structures of the newly found unreactive twisted form, PT-twist (a), and the reactive AP conformer of PT-OF (b).

with experimentally observed slow decay proceeding *via* an unspecified conformational change, reported for several different DAE systems.[81,82] Interestingly, a similar anti-parallel geometry was observed by Sotome *et al.* in an inverse DAE molecule with the same substituents (*i.e.*, with phenyl at positions 5 in the thiophene ring), and was considered nonreactive.[83] To determine the role of the PT-twist form in the PT-OF photodynamics, in the remaining part of the manuscript, we focus on the investigation of its possible relaxation pathways.

It should be kept in mind that the presented simulations are performed in the gas phase, while most experiments concerning the photophysics and photochemistry of DAE systems are performed in solution. This can have an impact on the possible relaxation pathways of the system, and the formed photoproducts. The viscosity of the solvent can hinder the conformational change from the PT-OF to PT-twist, decreasing the overall prevalence of this reaction channel. While the experimental data reporting fast ISC in DMPT was obtained in chloroform, which has a quite low viscosity, experiments conducted for different DAE switches[81,82] in high viscosity solvents (*cis*- and *trans*-decalin) show that the solvent viscosity can have an impact on the deactivation pathways of DAE systems. Aside from this, the presence of a solvent could also impact the transition energies in the studied DAE molecule (so called solvent shifts). The $S_0 \rightarrow S_1$ transition energies of all the ground-state and S_1 minima found in this study, with the several different solvents accounted for under the conductor-like screening model (COSMO),[84] are found in Table S8 of the ESI.† At this level of theory, the solvent has a negligible effect on the absorption properties of PT-CF; however, it adds an observable red-shift to the absorption maxima of the PT-OF and PT-twist, which increases with the dielectric constant of the solvent. At the same time, however, a parallel shift of the low-lying triplet state energies is observed. Eventually, it should be expected that, while the absolute transition energy values are sensitive to the environment, the proposed deactivation mechanism should be most likely prevalent in varying conditions, at least as long as they remain similar to the ones commonly chosen in DAE experiments.

3.3 Photophysics of the PT-twist

3.3.1 Relaxed properties of the S_0 and S_1 minimum-energy structures. Structural optimization performed at the ODM2/MRCI-SD level confirms that the PT-twist corresponds to a local minimum on the S_1 potential energy surface, with an adiabatic energy of 3.75 eV. This species is characterised by an elongated C_1–C_6 distance of 4.17 Å, and dihedral angles of φ_1 = 46 and φ_2 = 62 degrees (Fig. 6). Geometry optimization at the TD-DFT level of theory also locates an excited state minimum corresponding to the PT-twist, with the characteristic φ_1 and φ_2 dihedral angles taking smaller values of 12 and 25 degrees, respectively. Given the subtle, noncovalent character of interactions responsible for the thiophene ring orientation in the PT-twist, we predict this observed difference to originate from a different description of dispersion interactions in the two employed methods.[49,70]

Single-point QD-NEVPT2 calculations performed at the optimized PT-twist S_1-minimum reveal a small S_1–T_1 SOC-ME of 1.42 cm^{-1}, unlikely to facilitate an ISC to the triplet manifold of states directly, with a singlet–triplet energy gap, Δ_{ST}, of 0.13 eV. Interestingly, the S_1 and S_2 states are near-degenerate at this point, separated by 0.22 eV, with the wavefunction of the former comprising mainly the H–L configuration, and the latter composed predominantly of the H1–L configuration. Here, the HOMO and HOMO-1 orbitals are of π character and are localised on either of the thiophene rings, while the LUMO is a π* orbital localised on the C_3–C_4 double bond. The QD-NEVPT2 optimized orbital contours can be found in the ESI,† in Fig. S8. Higher triplet states, T_2 and T_3, are found to be almost-degenerate, and energetically above S_1 by about 0.2 eV. The SOC-ME between S_1 and T_2 and T_3 are found to be 2.84 cm^{-1} and 7.75 cm^{-1}.

A ground-state ODM2/MRCI-SD optimization starting from the PT-twist geometry reveals an additional S_0 minimum corresponding to this form, which has not been identified before. Here, the thiophene rings are almost perpendicular to the cyclopentyl plane, with φ_1 = 89 degrees and φ_2 = 113 degrees, and the C_1–C_6 amounts to 4.84 Å. The S_1 excitation energy at the S_0-optimized structure is found to be 4.90 eV, with a moderate oscillator strength of f = 0.0504, leading to the

H–L+1 orbital contribution. The S_2 and S_3 states are both bright, with oscillator strengths of f = 0.4041 and 0.3470, and with corresponding transition energies of 5.03 eV and 5.13 eV, respectively. Energetically, this new structure is almost degenerate with PT-OF: at the applied level of semi-empirical theory, it was found to lie even 0.04 eV lower. At the same time, it should be expected that the interaction between PT and typical solvents used in DAE experiments will stabilise the PT-OF form. Indeed, upon a single-point check performed at the ODM2/MRCI-SD level with the COSMO cyclohexane environment, the relative PT-twist form energy increases to +0.07 eV, remaining in line with the originally assumed global-minimum role of the PT-OF structure. Reoptimization at the DFT level yields a ground-state minimum of the PT-twist, with a relative energy of +0.28 eV with respect to the DFT-optimized PT-OF global minimum.

3.3.2 NAMD simulations of the PT-twist. To investigate the possibility of nonradiative decay of the PT-twist formed in the course of the PT-OF relaxation, NAMD simulations starting from geometries located around the S_1 PT-twist minimum were performed. The electronic state population evolution during these runs is found in Fig. S10 of the ESI.† In a simulated time frame of 2 ps, only 7% of trajectories relaxed to the ground state. Moreover, the saturated shape of state population curves indicates rather slow (or nonexistent) further nonradiative relaxation of the system, opening possibilities for an alternative deactivation channel. It might be of worth to note, though, that for the 9 trajectories of the PT-twist relaxing within the singlet manifold of states, the deactivation mechanism involves a bond-cleavage in the thiophene ring: either the C_1–C_2 (C_5–C_6) bond or the C_1 (C_6) C–S bond. At the same time, all relaxing trajectories form a photoproduct in the structural vicinity of the ground-state minimum of the PT-twist.

The observed photodynamics of the PT-twist can be compared with the experimental results by Hamdi *et al.*, reporting an ISC of the AP form in a very similar DAE system to occur within just 1 ps. This, along with no reported evidence for fluorescence originating from the AP form of PT or DMPT, and the slow or nonexistent internal conversion process of the PT-twist observed in NAMD simulations, leaves a vibration-mediated deactivation pathway through the triplet states as the most plausible deactivation mechanism of the PT-twist, which we investigate in more detail below.

3.3.3 Dynamic sampling of ISC effects. To account for the vibronic contribution to the ISC process in the PT-twist form, a dynamic sampling procedure, as described in the Methods section, was performed using data from the 125 NAMD trajectories calculated for the PT-twist. The analysis of the correlation between the characteristic PT geometrical parameters, C_3–C_4, φ_1, and φ_2, is shown in Fig. 7 in the form of heat maps. The values of particular geometric parameters of a given snapshot are denoted on the x and y axes, while the magnitude, taken as the average of all snapshots in a particular cell, of the SOC-ME between S_1 and T_1 is color-coded. To avoid biasing the results with low-probability structures, only cells containing more than 5 sampled conformations were plotted.

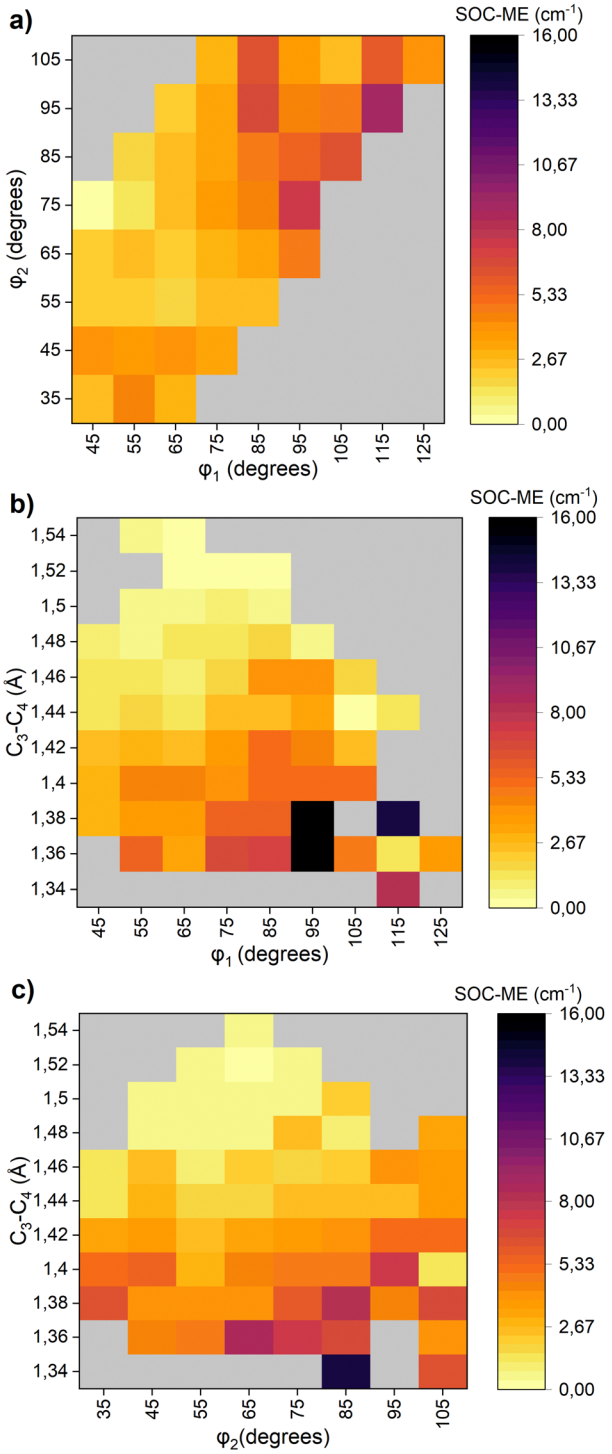

Fig. 7 Heat maps displaying the magnitude of the SOC-ME between the S_1 and T_1 states parametrized by geometric parameters of PT-OF: (a) dihedral angles φ_1 and φ_2, (b) dihedral angle φ_1 and the C_3–C_4 distance, and (c) dihedral angle φ_2 and the C_3–C_4 distance.

Due to the rather low energy gap between the S_1 singlet state and T_2 and T_3 triplet states, it is possible that ISC could occur in other triplet states than T_1. If a quantitative estimation of ISC time constants was to be performed, the effect of coupling between the S_1 and T_2 and T_3 should be taken into account.

However, the conducted study only aims at proving qualitatively the possibility of ISC during the cyclization reaction of PT (supporting available experimental data). Henceforth, we will only consider the ISC process from the S_1 state to the lowest lying triplet state, T_1.

First, focusing on the role of angles between the perfluoropentane ring and the thiophene moieties, φ_1 and φ_2 (Fig. 7a), one can notice that the magnitude of the SOC-ME peaks when one of the angles is equal to approximately 90 degrees, *i.e.*, when the planes of the perfluoro-pentane and the thiophene rings are orthogonal to each other. This leads to a negligible overlap between molecular orbitals of the two sub-systems, breaking the π-electronic conjugation.

Second, one can take a look at the correlation between the length of the central C_3–C_4 bond and the SOC-ME value shown in panels (b) and (c) of Fig. 7, with ϕ_1 and ϕ_2 angles marked on the *x* axis, respectively. From these plots, it can be immediately observed that a shorter C_3–C_4 distance favours a higher value of SOC-ME. This effect is particularly synergistic with the φ angle rotation, with SOC-ME reaching values well over 10 cm^{-1} when both of these parameters align.

The C_3–C_4 distance can be used as an indicator of the central cyclohexatriene bond character: smaller values, of about 1.35–1.40 Å, indicate a double bond, with an sp^2 hybridisation of C_3 and C_4, while larger values, of 1.45–1.55 Å, mean a single bond, with both the atoms sp^3-hybridised. It is worth mentioning that a phenomenon similar to the one discussed here has been observed previously, experimentally and theoretically, for phenylthiophene compounds.[85] Our findings are in line with the therein predicted increased quinoid-like character of the excited state (increase in the double-bond character of C_3–C_4), as well as the non-planarity of the excited state driving the intersystem crossing. The latter effect is known to impact spin–orbit coupling in other systems as well.[86,87]

Another key factor that needs to be take into account in order to estimate the rate of the intersystem crossing is the energy gap between the S_1 and T_1 states. In most cases, the Δ_{ST} value in the PT-twist dynamics is quite small, remaining below 0.50 eV. Moreover, sometimes the singlet–triplet energy difference even drops to a negative value, indicating a vibrationally induced Hund's rule violation. Color-coded heat maps, analogous to the SOC maps, illustrating the dependence of Δ_{ST} on the same geometric parameters are found in Fig. S11 in the ESI.† Overall, while the energy gap might be higher in some regions exhibiting particularly strong SOC, the PT system does not show a general correlation between Δ_{ST} and the magnitude of SOC-ME: in fact, there are plenty of sample points with SOC-ME well above 10 cm^{-1} and Δ_{ST} below 0.20 eV, as illustrated in Fig. 8.

The observed vibrationally induced increase of the SOC-ME and, hence, the expected enhanced ISC rate can also be interpreted in terms of El-Sayed's rules,[88,89] stating that "the rate of intersystem crossing is relatively large if the radiationless transition involves a change of orbital type".[90] Here, the orbital type refers to its symmetry. In Fig. 9, one can find the QD-NEVPT2 orbital contours of an example sampling the snapshot

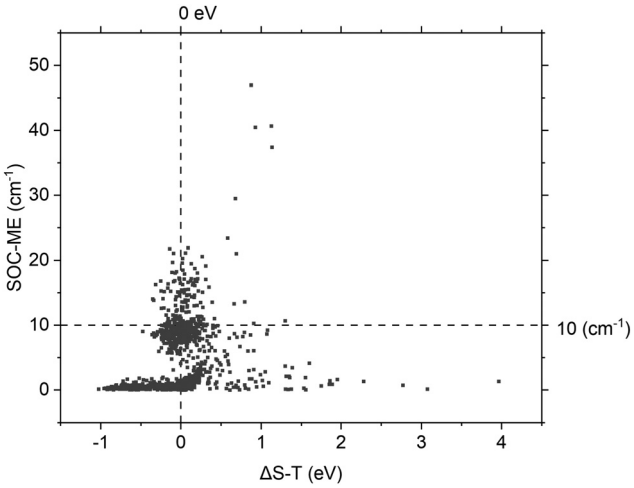

Fig. 8 Correlation plot illustrating the magnitude of the SOC-ME and energy gap between the S_1 and T_1 states in the computed snapshots.

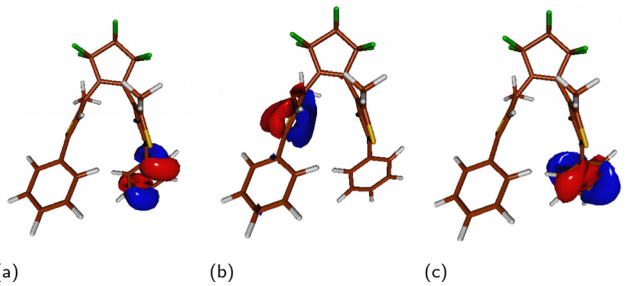

Fig. 9 HOMO (a), LUMO (b), and LUMO+1 (c) orbital contours of the PT-twist optimized at a sample point exhibiting high spin–orbit coupling.

with a high SOC-ME value. In this case, the T_1 state's wavefunction is composed mainly of a H–L determinant, while S_1 is of the H–L1 character. Both the HOMO and the LUMO+1 orbital are centred on the phenyl ring which tends to orient perpendicularly to the thiophene rings, while the LUMO is located on the thiophene moiety of the opposite aryl substituent. Thus, while the HOMO and LUMO+1 orbitals share the same plane of symmetry, the LUMO is symmetric with respect to an approximately orthogonal plane of the thiophene ring. As a result, a transition from the H–L+1 singlet state to the H–L triplet state involves a change of orbital symmetry and, following the El-Sayed rules, is predicted to provide an efficient pathway for the ISC process.

Eventually, considering all the points discussed above, and taking into account the experimental evidence for ultrafast ISC in closely related DAE systems,[36] we are inclined to assume the $S_1 \rightarrow T_1$ ISC as the leading S_1 decay mechanism for the PT-twist isomer.

Finally, to elucidate the fate of the system after the ISC process, an optimization of the T_1 state was performed, at the ODM2/MRCI-SD level, starting from the S_1 minimum of the PT-twist. The optimization yields a structure without major geometric rearrangements, with the only substantial difference being the increased piramidization of the C_1 carbon atom.

Here, the triplet state is of the H–L+1 character, with both orbitals delocalized over the entire phenylthiophene moiety, giving the potential $T_1 \rightarrow S_0$ transition a local character. The Cartesian coordinates of the optimized triplet state, as well as the ODM2/MRCI-SD orbitals, can be found in the ESI,† in Table S15 and Fig. S5, respectively. The adiabatic energy of the T_1 state is predicted to be 2.41 eV, with a T_1/S_0 energy gap of 1.35 eV (918 nm). This value seems to underestimate the phosphorescence energy by *ca.* 0.4 eV with respect to the experimentally reported, wide phosphorescence spectrum[36] which, however, remains within the average accuracy of the ODM2/MRCI-SD method applied to DAE systems.

4 Conclusions

The ring-closure reaction of a popular diarylethene photoswitch, PT, was studied by means of the on-the-fly nonadiabatic molecular dynamics simulations. The conducted simulations allowed the available experimental results to be replicated with satisfactory accuracy as well as provided novel insights into the photo-relaxation mechanism of the open-ring PT form. Using a dynamic configuration-space sampling procedure, we identified the key forms and structural changes involved in the experimentally observed triplet deactivation pathway in dithienylethene molecules undergoing the photo-cyclization reaction. The spatial orientation of the thiophene rings as well as the character of the central bond in the hexatriene moiety were found to strongly influence the magnitude of the spin–orbit coupling. An additional singlet-mediated reaction pathway proceeding *via* proton/hydrogen atom transfer was identified and characterised. Our findings, on the one hand, support and rationalise the available experimental data on DAE photoswitches and, on the other hand, provide information that can guide the rational design of diarylethene systems for both fundamental research and technological applications.

Author contributions

Mikołaj Martyka: writing – original draft, writing – review and editing, visualization, investigation, formal analysis, data curation, methodology, conceptualization, and software. Joanna Jankowska: writing – review and editing, validation, supervision, project administration, methodology, investigation, funding acquisition, and conceptualization.

Conflicts of interest

There are no conflicts to declare.

Acknowledgements

The authors thank the National Science Centre (Poland) for financial support through grant 2018/31/D/ST4/02219. The Polish high-performance computing infrastructure, PLGrid (HPC Centers: ACK Cyfronet AGH), is also gratefully acknowledged for providing computer facilities and support through computational grant no. PLG/2023/016751.

Notes and references

1 Y. Nakagawa, T. Hishida, K. Sumaru, K. Morishita, K. Kirito, S. Yokojima, Y. Sakamoto, S. Nakamura and K. Uchida, *J. Med. Chem.*, 2023, **66**, 5937–5949.
2 M. Yin, Q. Zhang, T. Fan, C. Fan, S. Pu, R. Krishna and F. Luo, *Chem. Eng. J.*, 2023, **451**, 139004.
3 L. Mao, H. Ding, X. Li, G. Liu and S. Pu, *J. Photochem. Photobiol., A*, 2022, **431**, 114011.
4 Y. Chen, H. Wang, H. Chen, W. Zhang, S. Xu, M. Pätzel, C. Ma, C. Wang, I. McCulloch, S. Hecht and P. Samorì, *Adv. Funct. Mater.*, 2023, 2305494.
5 Y.-Y. Tang, Y.-L. Zeng and R.-G. Xiong, *J. Am. Chem. Soc.*, 2022, **144**, 8633–8640.
6 S. Takami, S. Kobatake, T. Kawai and M. Irie, *Chem. Lett.*, 2003, **32**, 892–893.
7 H. Jean-Ruel, R. R. Cooney, M. Gao, C. Lu, M. A. Kochman, C. A. Morrison and R. J. D. Miller, *J. Phys. Chem. A*, 2011, **115**, 13158–13168.
8 H. Jean-Ruel, M. Gao, M. A. Kochman, C. Lu, L. C. Liu, R. R. Cooney, C. A. Morrison and R. J. D. Miller, *J. Phys. Chem. B*, 2013, **117**, 15894–15902.
9 K. Uno, M. L. Bossi, V. N. Belov, M. Irie and S. W. Hell, *Chem. Commun.*, 2020, **56**, 2198–2201.
10 R. J. D. Miller, *Science*, 2014, **343**, 1108–1116.
11 C. R. Honick, G. M. Peters, J. D. Young, J. D. Tovar and A. E. Bragg, *Phys. Chem. Chem. Phys.*, 2020, 17–21.
12 M. Irie, T. Fukaminato, K. Matsuda and S. Kobatake, *Chem. Rev.*, 2014, **114**, 12174–12277.
13 Z. Li, J. Xia, J. Liang, J. Yuan, G. Jin, J. Yin, G. A. Yu and S. H. Liu, *Dyes Pigm.*, 2011, **90**, 290–296.
14 M. Irie, T. Lifka, S. Kobatake and N. Kato, *J. Am. Chem. Soc.*, 2000, **122**, 4871–4876.
15 K. Shibata, K. Muto, S. Kobatake and M. Irie, *J. Phys. Chem. A*, 2002, **106**, 209–214.
16 M. Irie, *Diarylethene molecular photoswitches concepts and functionalities*, Wiley-VCH, Weinheim, 2021.
17 M. Hanazawa, R. Sumiya, Y. Horikawa and M. Irie, *J. Chem. Soc., Chem. Commun.*, 1992, 206–207.
18 A. J. Vazquez and N. S. Nudelman, *J. Phys. Org. Chem.*, 2012, **25**, 925–932.
19 Y. Ishibashi, M. Fujiwara, T. Umesato, H. Saito, S. Kobatake, M. Irie and H. Miyasaka, *J. Phys. Chem. C*, 2011, **115**, 4265–4272.
20 Y. Ishibashi, T. Umesato, M. Fujiwara, K. Une, Y. Yoneda, H. Sotome, T. Katayama, S. Kobatake, T. Asahi, M. Irie and H. Miyasaka, *J. Phys. Chem. C*, 2016, **120**, 1170–1177.
21 R. B. Woodward and R. Hoffmann, *J. Am. Chem. Soc.*, 1965, **87**, 395–397.
22 R. B. Woodward and R. Hoffmann, *Angew. Chem., Int. Ed. Engl.*, 1969, **8**, 781–853.

23 H. Sotome, T. Nagasaka, K. Une, S. Morikawa, T. Katayama, S. Kobatake, M. Irie and H. Miyasaka, *J. Am. Chem. Soc.*, 2017, **139**, 17159–17167.
24 H. Sotome, H. Okajima, T. Nagasaka, Y. Tachii, A. Sakamoto, S. Kobatake, M. Irie and H. Miyasaka, *ChemPhysChem*, 2020, **21**, 1524–1530.
25 M. Herder, B. M. Schmidt, L. Grubert, M. Pätzel, J. Schwarz and S. Hecht, *J. Am. Chem. Soc.*, 2015, **137**, 2738–2747.
26 J. L. Butterfield, G. P. Penoncello, K. Dikshit and C. J. Bruns, *ACS Appl. Nano Mater.*, 2022, **5**, 13840–13844.
27 Y. Akaishi, A. D. Pramata, S. Tominaga, S. Kawashima, T. Fukaminato and T. Kida, *Chem. Commun.*, 2019, **55**, 8060–8063.
28 K. Zheng, S. Han, X. Zeng, Y. Wu, S. Song, H. Zhang and X. Liu, *Adv. Mater.*, 2018, **30**, 1–5.
29 J. J. De Jong, W. R. Browne, M. Walko, L. N. Lucas, L. J. Barrett, J. J. McGarvey, J. H. Van Esch and B. L. Feringa, *Org. Biomol. Chem.*, 2006, **4**, 2387–2392.
30 H. Shoji, D. Kitagawa and S. Kobatake, *New J. Chem.*, 2014, **38**, 933–941.
31 D. Kitagawa, T. Nakahama, Y. Nakai and S. Kobatake, *J. Mater. Chem. C*, 2019, **7**, 2865–2870.
32 H. Sotome, K. Une, T. Nagasaka, S. Kobatake, M. Irie and H. Miyasaka, *J. Chem. Phys.*, 2020, **152**, 034301.
33 K. Morimitsu, S. Kobatake and M. Irie, *Mol. Cryst. Liq. Cryst.*, 2005, **431**, 451–454.
34 P. R. Hania, R. Telesca, L. N. Lucas, A. Pugzlys, J. van Esch, B. L. Feringa, J. G. Snijders and K. Duppen, *J. Phys. Chem. A*, 2002, **106**, 8498–8507.
35 E. Pontecorvo, C. Ferrante, C. G. Elles and T. Scopigno, *J. Phys. Chem. B*, 2014, **118**, 6915–6921.
36 I. Hamdi, G. Buntinx, A. Perrier, O. Devos, N. Jaïdane, S. Delbaere, A. K. Tiwari, J. Dubois, M. Takeshita, Y. Wada and S. Aloïse, *Phys. Chem. Chem. Phys.*, 2016, **18**, 28091–28100.
37 S. Nakamura and M. Irie, *J. Org. Chem.*, 1988, **53**, 6136–6138.
38 D. Majumdar, H. M. Lee, J. Kim, K. S. Kim and B. J. Mhin, *J. Chem. Phys.*, 1999, **111**, 5866–5872.
39 K. Uchida, D. Guillaumont, E. Tsuchida, G. Mochizuki, M. Irie, A. Murakami and S. Nakamura, *THEOCHEM*, 2002, **579**, 115–120.
40 Y. Asano, A. Murakami, T. Kobayashi, A. Goldberg, D. Guillaumont, S. Yabushita, M. Irie and S. Nakamura, *J. Am. Chem. Soc.*, 2004, **126**, 12112–12120.
41 A. Perrier, S. Aloise, M. Olivucci and D. Jacquemin, *J. Phys. Chem. Lett.*, 2013, **4**, 2190–2196.
42 M. G. Chiariello, U. Raucci, F. Coppola and N. Rega, *Phys. Chem. Chem. Phys.*, 2019, **21**, 3606–3614.
43 E. Salazar, S. Reinink and S. Faraji, *Phys. Chem. Chem. Phys.*, 2022, **24**, 11592–11602.
44 J. Jankowska, M. Martyka and M. Michalski, *J. Chem. Phys.*, 2021, **154**, 204305.
45 M. Boggio-Pasqua, M. Ravaglia, M. J. Bearpark, M. Garavelli and M. A. Robb, *J. Phys. Chem. A*, 2003, **107**, 11139–11152.
46 C. Wiebeler and S. Schumacher, *J. Phys. Chem. A*, 2014, **118**, 7816–7823.
47 A. Jarota, E. Pastorczak and H. Abramczyk, *Phys. Chem. Chem. Phys.*, 2020, **22**, 5408–5412.
48 M. Martyka and J. Jankowska, *J. Photochem. Photobiol., A*, 2023, **438**, 114513.
49 P. O. Dral, X. Wu, L. Spörkel, A. Koslowski, W. Weber, R. Steiger, M. Scholten and W. Thiel, *J. Chem. Theory Comput.*, 2016, **12**, 1082–1096.
50 A. Koslowski, M. E. Beck and W. Thiel, *J. Comput. Chem.*, 2003, **24**, 714–726.
51 W. Weber and W. Thiel, *Theor. Chem. Acc.*, 2000, **103**, 495–506.
52 P. O. Dral, X. Wu and W. Thiel, *J. Chem. Theory Comput.*, 2019, **15**, 1743–1760.
53 W. Thiel, *MNDO99 v7.0 with upgrades*, Max-Planck-Institut für Kohlenforschung, 2017.
54 M. R. Silva-Junior and W. Thiel, *J. Chem. Theory Comput.*, 2010, **6**, 1546–1564.
55 G. Cui and W. Thiel, *Angew. Chem., Int. Ed.*, 2013, **52**, 433–436.
56 Y.-J. Gao, X.-P. Chang, X.-Y. Liu, Q.-S. Li, G. Cui and W. Thiel, *J. Phys. Chem. A*, 2017, **121**, 2572–2579.
57 Y. Lu, Z. Lan and W. Thiel, *Angew. Chem., Int. Ed.*, 2011, **50**, 6864–6867.
58 J. B. Schönborn, A. Koslowski, W. Thiel and B. Hartke, *Phys. Chem. Chem. Phys.*, 2012, **14**, 12193–12201.
59 J. B. Schönborn and B. Hartke, *Phys. Chem. Chem. Phys.*, 2014, **16**, 2483–2490.
60 M. J. S. Dewar, J. A. Hashmall and C. G. Venier, *J. Am. Chem. Soc.*, 1968, **90**, 1953–1957.
61 C. Angeli, R. Cimiraglia, S. Evangelisti, T. Leininger and J.-P. Malrieu, *J. Chem. Phys.*, 2001, **114**, 10252–10264.
62 C. Angeli, R. Cimiraglia and J.-P. Malrieu, *J. Chem. Phys.*, 2002, **117**, 9138–9153.
63 F. Neese, *Wiley Interdiscip. Rev.: Comput. Mol. Sci.*, 2012, **2**, 73–78.
64 F. Neese, *Wiley Interdiscip. Rev.: Comput. Mol. Sci.*, 2018, **8**, e1327.
65 T. H. Dunning, *J. Chem. Phys.*, 1989, **90**, 1007–1023.
66 G. L. Stoychev, A. A. Auer and F. Neese, *J. Chem. Theory Comput.*, 2017, **13**, 554–562.
67 B. A. Heß, C. M. Marian, U. Wahlgren and O. Gropen, *Chem. Phys. Lett.*, 1996, **251**, 365–371.
68 J. Tatchen and C. M. Marian, *Chem. Phys. Lett.*, 1999, **313**, 351–357.
69 F. Neese, *J. Chem. Phys.*, 2005, **122**, 034107.
70 J.-D. Chai and M. Head-Gordon, *Phys. Chem. Chem. Phys.*, 2008, **10**, 6615–6620.
71 S. Hirata and M. Head-Gordon, *Chem. Phys. Lett.*, 1999, **314**, 291–299.
72 J. C. Tully, *J. Chem. Phys.*, 1990, **93**, 1061–1071.
73 S. Hammes-Schiffer and J. C. Tully, *J. Chem. Phys.*, 1994, **101**, 4657–4667.
74 G. J. Martyna, M. L. Klein and M. Tuckerman, *J. Chem. Phys.*, 1992, **97**, 2635–2643.
75 M. Barbatti, G. Granucci, M. Persico, M. Ruckenbauer, M. Vazdar, M. Eckert-Maksić and H. Lischka, *J. Photochem. Photobiol., A*, 2007, **190**, 228–240.
76 E. Fabiano, T. Keal and W. Thiel, *Chem. Phys.*, 2008, **349**, 334–347.
77 L. Spörkel and W. Thiel, *J. Chem. Phys.*, 2016, **144**, 194108.

78 J. E. Subotnik and N. Shenvi, *J. Chem. Phys.*, 2011, **134**, 024105.
79 S. Wallis, *J. Quant. Linguist.*, 2013, **20**, 178–208.
80 L. Spörkel, J. Jankowska and W. Thiel, *J. Phys. Chem. B*, 2015, **119**, 2702–2710.
81 H. Miyasaka, T. Nobuto, M. Murakami, A. Itaya, N. Tamai and M. Irie, *J. Phys. Chem. A*, 2002, **106**, 8096–8102.
82 Y. Ishibashi, M. Fujiwara, T. Umesato, H. Saito, S. Kobatake, M. Irie and H. Miyasaka, *J. Phys. Chem. C*, 2011, **115**, 4265–4272.
83 H. Sotome, D. Kitagawa, T. Nakahama, S. Ito, S. Kobatake, M. Irie and H. Miyasaka, *Phys. Chem. Chem. Phys.*, 2019, **21**, 8623–8632.
84 A. Klamt and G. Schüürmann, *J. Chem. Soc., Perkin Trans. 2*, 1993, 799–805.
85 I. L. Zheldakov, J. M. Wasylenko and C. G. Elles, *Phys. Chem. Chem. Phys.*, 2012, **14**, 6211.
86 F. D. Lewis and X. Zuo, *J. Am. Chem. Soc.*, 2003, **125**, 8806–8813.
87 N. I. Nijegorodov and W. S. Downey, *J. Phys. Chem.*, 1994, **98**, 5639–5643.
88 M. A. El-Sayed, *Acc. Chem. Res.*, 1968, **1**, 8–16.
89 M. El-Sayed, *J. Chem. Phys.*, 1963, **38**, 2834–2838.
90 IUPAC, *Compendium of Chemical Terminology, (the "Gold Book")*, Blackwell Scientific Publications, 2nd edn, 1997.

